



Contents lists available at ScienceDirect

## International Journal of Mechanical Sciences

journal homepage: [www.elsevier.com/locate/ijmecsci](http://www.elsevier.com/locate/ijmecsci)

# TPMS-infill MMC-based topology optimization considering overlapped component property

Sinuo Zhang<sup>a</sup>, Daicong Da<sup>b</sup>, Yingjun Wang<sup>a,c,\*</sup>

<sup>a</sup> National Engineering Research Center of Novel Equipment for Polymer Processing, The Key Laboratory of Polymer Processing Engineering of the Ministry of Education, Guangdong Provincial Key Laboratory of Technique and Equipment for Macromolecular Advanced Manufacturing, South China University of Technology, Guangzhou 510641, China

<sup>b</sup> Department of Mechanical Engineering, Northwestern University, Evanston, IL 60208, United States

<sup>c</sup> State Key Laboratory of Digital Manufacturing Equipment and Technology, Huazhong University of Science and Technology, Wuhan 430074, China

## ARTICLE INFO

## Keywords:

Engineering design  
Architected materials  
Triply periodic minimal surface  
Topology optimization  
Multiple materials

## ABSTRACT

Engineering designs involving multiple materials suffer either difficult interface modeling or finding physically meaningful transition domains with a clear or even optimal structural representation. However, previous material interpolation models often cannot achieve either of them. A new function interpolation scheme is proposed in this work by leveraging the triply periodic minimal surfaces (TPMS). This TPMS-based architecture will serve as the infill morphology at the microstructural scale, while its distribution at the higher structural scale will be achieved by topology optimization (TO). The moving morphable component (MMC)-based TO is adopted to first reduce the number of design variables and then provide explicit structural geometries. For finite elements where multiple materials exist (or the overlapping component area), level set functions are constructed to identify the interpolation parameters to determine the TPMS with clear material characteristics. This framework will thus allow us to generate new architected materials associated with the optimized design variable at the structural scale, while guaranteeing a smooth and meaningful transition at lower material microstructures. Numerical examples show that stress concentration can be significantly reduced because of the distinguished compatibility inside the heterogeneous structure, which leads to its successful manufacturing by the 3D printing. Finally, a real engineering case for the design of an automotive connecting rod is presented to illustrate the versatility of the proposed approach.

## 1. Introduction

Triply periodic minimal surfaces (TPMS), which widely exist in the natural world especially in biological tissues [1–3], have a state with minimum energy under finite boundary conditions. Their superior mechanical and many other multi-functional properties attract great interest from researchers. The feature we leverage most in this work is that TPMSs can be expressed parametrically to be optimally designed. Due to this property, the transition between two different architectures can easily be implemented. These periodic structural architectures that can be expressed parametrically have already been proven to have significant advantages in solving certain challenges, e.g. the quarter unit cells with rectangular holes close to rank- $n$  laminates are suitable for stiffness optimization [4]. TPMSs are also combined with the Generative Adversarial Network-based Machine Learning techniques [5] in the

context of inverse homogenization design for metamaterials and structures. In addition to that, TPMSs also have other useful attributions such as high surface-to-volume ratio [6], good inner-connectivity [7], high specific strength and stiffness to relatively low mass [8,9], and optimal fluid permeability [10]. This type of architecture has a wide scope of development in tissue engineering, biomedical science, material science, and other engineering fields. In this work, TPMSs are introduced here to be the infill microstructures for the multiscale engineering design, specifically the structural topology optimization (TO). Their implicit function expressions are interpolated to synthesize new TPMSs for the connection area of different materials, so that the accurate structural description can be obtained. The optimized properties of the corresponding parts will also be acquired correspondingly.

TO, one of the most intelligent structural optimization methods, focuses on obtaining the optimal material distribution within a prescribed

\* Corresponding author.

E-mail address: [wangyj84@scut.edu.cn](mailto:wangyj84@scut.edu.cn) (Y. Wang).

<https://doi.org/10.1016/j.ijmecsci.2022.107713>

Received 22 April 2022; Received in revised form 31 August 2022; Accepted 31 August 2022

Available online 6 September 2022

0020-7403/© 2022 Elsevier Ltd. All rights reserved.

design domain under given constraints. Since the pioneering work of Bendsøe and Kikuchi [11], numerous TO approaches have been proposed, such as solid isotropic material with penalization (SIMP) [12,13], level set [14,15], evolutionary structural optimization (ESO) [16] and its variants [17,18], and isogeometric analysis (IGA) [19,20], etc [21]. These methods have been widely used in a series of engineering [22–26].

In addition to the TO methods mentioned above, Guo et al. [27,28] proposed a novel TO method through moving morphable components (MMC). It uses the topology description function (TDF) to describe the layout, position, and geometry features of components and achieved optimized topology by optimizing the parameters of components. Compared with some traditional TO approaches, the MMC method significantly reduces the number of design variables and provides more explicit geometries. It thereby attracts extensive attention in TO. Zhang et al. [29] used the MMC framework to solve the multi-materials TO problems and proposed a method to reduce the number of degrees of freedom in finite element analysis. Xie et al. [30] proposed a new TO approach combining the MMC-based TO with IGA. To solve the  $C^1$  discontinuity problem of the component-overlapping parts, which may lead to the objective function non-differentiable, an R-function is introduced to represent the TDF to improve the convergence rate. Liu et al. [31] proposed an efficient MMC-based method for multi-resolution TO, which can obtain a high-resolution result with fewer design variables and degrees of freedom. Based on the above advantages, our study is built on the MMC-based TO framework.

With the power of additive manufacturing technology which is able to control the architecture at the small scale multi-material and multi-scale TO is attracting more and more attention. The multi-material TO aims to find an optimal distribution of different types of materials in a given condition, which can take full advantage of the properties of various materials in a targeted manner to meet complex engineering requirements [32,33]. Interfacial effects between different phases on crack propagation and design of fracture-resistant interfaces are studied in [34]. Multi-scale multi-material TO optimizes the architectures at two different scales simultaneously [35,36] and aims to provide better mechanical performance [36–41]. Wang et al [42] proposed a cross-scale robust TO approach that considers the uncertainties of loads, and they used the filer-projection technique to obtain better micro-configuration and improve the manufacturability. One of the key issues in multi-material and multi-scale TO problems is to define the suitable transition between different materials, while the previous interpolation schemes often cannot solve the problem. Bendsøe and Sigmund [43] used an interpolation scheme based on a rule of mixtures to represent the distribution of multiple materials. With the use of this interpolation approach, the SIMP method needs  $n - 1$  density functions to represent  $n$  material phases. Then, many improved material interpolation methods were proposed under the SIMP approach [44–46]. In the level set framework, Wang et al. [47,48] proposed a multi-phase model called "color" level-set representation for the multi-material TO, which could substantially reduce the number of model functions especially when the material phases become large. This approach has been generalized and well applied to many multi-material TO problems [49,50]. Wang et al. [51] proposed a multi-material TO method based on the material-field series-expansion model, which introduces several individual material fields to represent the distribution of materials. This method significantly reduced the number of design variables and gave the optimization formulation without additional constraints. However, since most of the previous methods only considered how to numerically approximate the material properties of these parts, they cannot provide an explicit architecture for the transition or overlapped parts for different materials. Thus, it is necessary to find a way to efficiently represent the transition area by using distinguished structural architectures with clear material characteristics.

This paper proposes a TPMSs-infill multi-microstructures TO approach based on the MMC framework, where the properties of the

overlapped components with multiple materials are taken into account. A TPMS implicit function interpolation scheme is proposed to provide explicit descriptions of structures in the overlapped parts. To do so, the Fourier expressions of TPMSs are interpolated, and the synthesized TPMS formulations are combined with the topological description of the components in MMC framework. During the TO, the morphology of infill microstructures will be adjusted with the overlap of multiple materials. Meanwhile, the properties of different composed microstructures are measured and fitted before the TO process, so that the performance parameters and the determined infill microstructure of the elements can be obtained. Utilizing the performances of TPMS, the discontinuity and high-stress concentration issues caused by the microstructural mismatch in the multi-material can be overcome, and a smooth transition between different materials is achieved.

The remainder of this paper is organized as follows. Firstly, the framework of MMC-based TO and the way of generating TPMSs are presented in Section 2. Next, key techniques that enable the implementation of the proposed design optimization framework are introduced in Section 3. This includes the interpolation scheme for generating new structures, finite element analysis, the method of combining microstructural morphology with element information, as well as the sensitivity analysis. This section will also provide a flowchart of the proposed algorithm and will be followed by some numerical examples in Section 4. Both 2D and 3D examples are presented in Section 4 to illustrate the effectiveness of the proposed design methodology. Real-world manufacturing and engineering design cases demonstrate the practical usefulness of the work presented. This paper concludes in Section 5.

## 2. Theoretical background

MMC-based TO and TPMS are the theoretical backgrounds of this paper. In this section, the general framework of MMC-based TO and some basic theories of TPMS are introduced. We refer readers to [52,53] for more detailed discussions.

### 2.1. The framework of MMC-based topology optimization

In the MMC-based approach, there are several components embedded in the specific domain. As shown in Guo et al. [54,55], the geometry of a component can be represented by the Eulerian description-based approach. The following Eulerian description functions provide flexible parameters to describe both the geometry of 2D and 3D components. For the 2D component, we have:

$$\phi_i(x, y) = \left(\frac{x'}{L}\right)^p + \left(\frac{y'}{g(x')}\right)^p - 1 \quad (1)$$

with

$$\begin{Bmatrix} x' \\ y' \end{Bmatrix} = \begin{bmatrix} c_r & s_r \\ -s_r & c_r \end{bmatrix} \begin{Bmatrix} x - x_0 \\ y - y_0 \end{Bmatrix} \quad (2)$$

For the 3D component, we have:

$$\phi_i(x, y, z) = 1 - \left(\frac{x'}{L}\right)^p - \left(\frac{y'}{g(x')}\right)^p - \left(\frac{z'}{f(x', y')}\right)^p \quad (3)$$

with

$$\begin{Bmatrix} x' \\ y' \\ z' \end{Bmatrix} = \begin{bmatrix} R_{11} & R_{12} & R_{13} \\ R_{21} & R_{22} & R_{23} \\ R_{31} & R_{23} & R_{33} \end{bmatrix} \begin{Bmatrix} x - x_0 \\ y - y_0 \\ z - z_0 \end{Bmatrix} \quad (4)$$

and

$$\begin{bmatrix} R_{11} & R_{12} & R_{13} \\ R_{21} & R_{22} & R_{23} \\ R_{31} & R_{32} & R_{33} \end{bmatrix} = \begin{bmatrix} c_b \cdot c_t & -c_b \cdot s_t & s_b \\ s_a \cdot s_b \cdot c_t + c_a \cdot s_t & -s_a \cdot s_b \cdot s_t + c_b \cdot c_t & -s_a \cdot c_b \\ -c_a \cdot s_b \cdot c_t + s_b \cdot s_t & c_a \cdot s_b \cdot s_t + s_a \cdot c_t & c_a \cdot c_b \end{bmatrix} \quad (5)$$

where  $s_a = \sin\alpha$ ,  $s_b = \sin\beta$ ,  $s_t = \sin\theta$ ,  $c_a = \sqrt{1 - s_a^2}$ ,  $c_b = \sqrt{1 - s_b^2}$ , and  $c_t = \sqrt{1 - s_t^2}$ .  $\alpha$ ,  $\beta$ ,  $\theta$  are the inclined angles of a component from the global coordinate system  $o$ - $x$ - $y$ - $z$  to the local coordinate system. In Eqs. (1) and (3),  $p$  is an even integer number, and we take  $p = 6$  in this study [29]. Coordinates  $(x_0, y_0)$  and  $(x_0, y_0, z_0)$  are the center of 2D and 3D components, respectively, and the symbol  $L$  denotes the half-length of the component. The shape parameters of a component, including thickness and width, are determined by  $g(x')$  and  $f(x', y')$ , respective, which can be expressed as:

$$g(x') = \frac{h_1 + h_2 - 2h_3}{2(L)^2} (x')^2 + \frac{h_2 - h_1}{2L} x' + h_3 \quad (6)$$

$$f(x', y') = \frac{t_1 + t_2 - 2t_3}{2(g(x'))^2} (y')^2 + \frac{t_2 - t_1}{2g(x')} y' + t_3 \quad (7)$$

$h_i$  and  $t_i$  are the thickness in  $y$  and  $z$  directions, respectively. A schematic diagram of the geometric description of the 2D and 3D structural components is shown in Fig. 1.

Another issue for presenting the component is to achieve the TDF.

Under the framework of MMC, the following level set function can be used to describe the region  $\Omega$  occupied by a component in a given design domain  $D$  (see Fig. 2(a) for reference):

$$\begin{cases} \phi(x) > 0, \forall x \in \Omega \\ \phi(x) = 0, \forall x \in \partial\Omega \\ \phi(x) < 0, \forall x \in D \setminus (\Omega \cup \partial\Omega) \end{cases} \quad (8)$$

If there are  $n$  components in the design domain, the TDF for components could be expressed as:

$$\begin{cases} \phi^s(x) > 0, \forall x \in \Omega^s \\ \phi^s(x) = 0, \forall x \in \partial\Omega^s \\ \phi^s(x) < 0, \forall x \in D \setminus (\Omega^s \cup \partial\Omega^s) \end{cases} \quad (9)$$

where  $\phi^s = \max(\phi_1, \dots, \phi_j, \dots, \phi_n)$  with  $\phi_j, j = 1, \dots, n$  represents the TDF of  $j$ -th component.  $\Omega^s = \bigcup_{j=1}^n \Omega_j$  is the region infilled with all the components. Supposing there are  $m$  types of materials introduced in the optimization problem, the components can be divided into  $m$  groups. All components composed of the same material belong to the same group. The TDF of the region occupied by  $i$ -th material could be correspondingly described as:

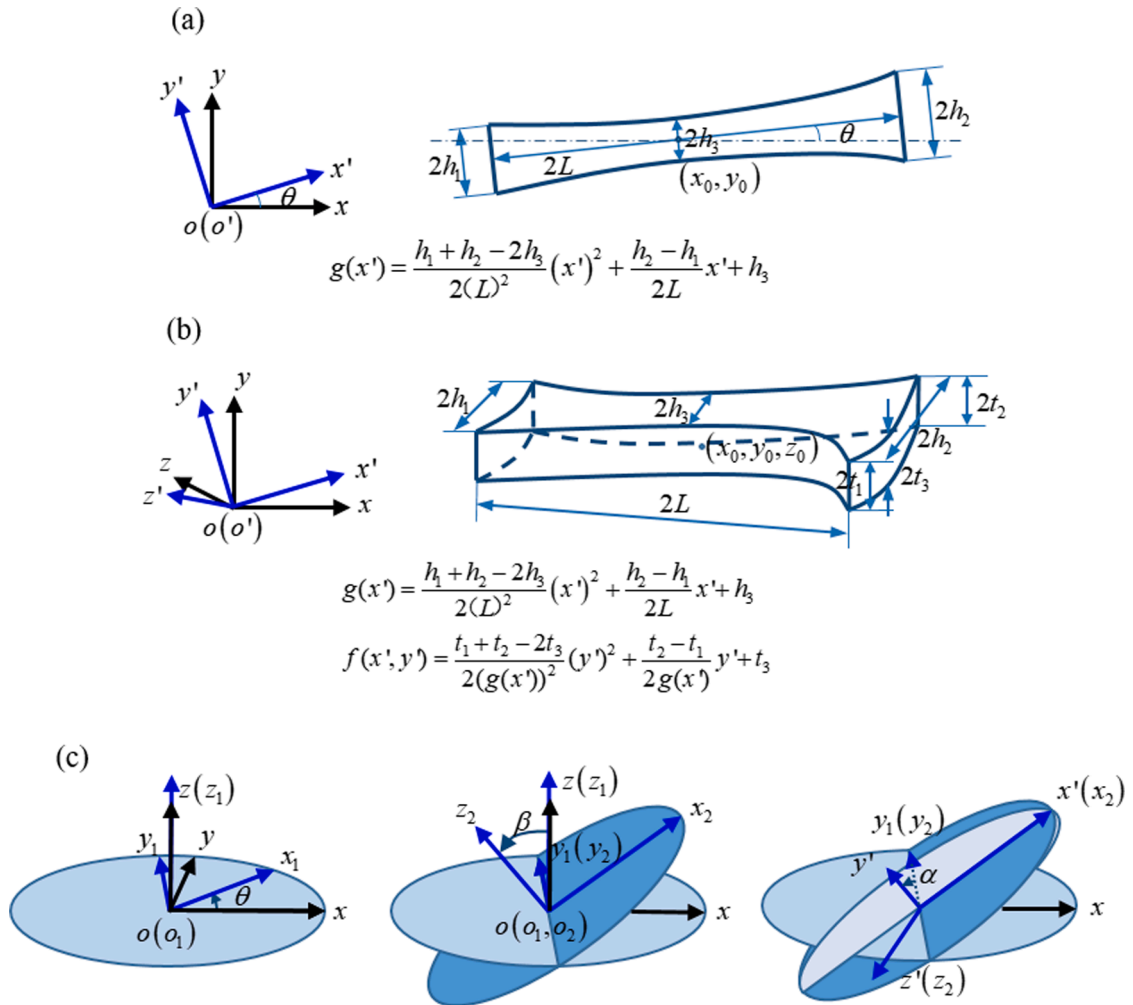
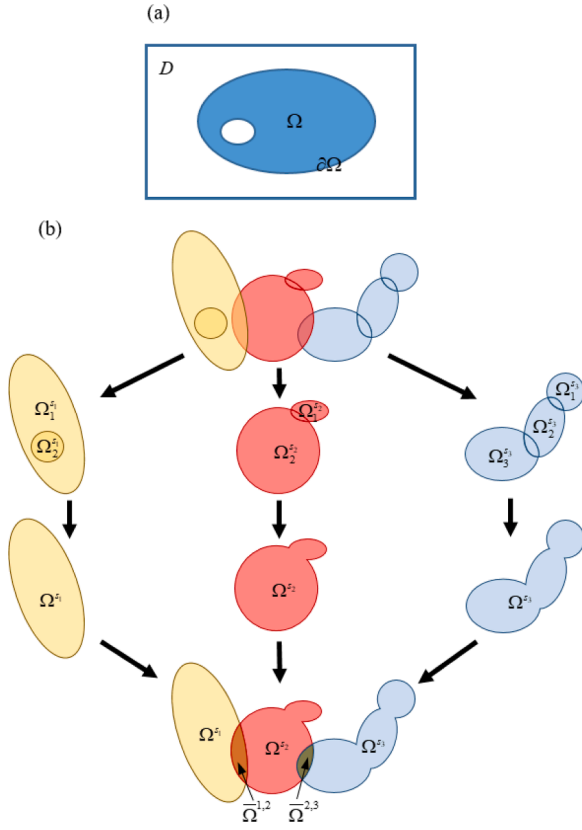


Fig. 1. A geometry description of 2D and 3D components: (a) a two-dimensional component and its geometric description function; (b) a three-dimensional component and its geometric description functions; (c) a schematic illustration of the rotation transformation. The global coordinate system  $o$ - $x$ - $y$ - $z$  is represented in black color and the local coordinate systems are shown in blue. The rotation angles  $\alpha$ ,  $\beta$ ,  $\theta$  rotate from the global coordinate system to the local coordinate systems.



**Fig. 2.** A schematic illustration of the topology description under the proposed method: (a) region of two-phase materials as represented by the level-set function. The symbol  $D$  represents the region of the design domain.  $\Omega$  is the region occupied by solid material and  $\partial\Omega$  is the boundary of  $\Omega$ ; (b) process of constructing  $\Omega^i$  and  $\bar{\Omega}$ . The three different materials are represented in yellow, red, and blue colors, respectively.  $\Omega_j^i$  represents the  $j$ -th components made of material  $i$  and  $\Omega^i$  denotes the region composed of material  $i$ .  $\bar{\Omega}^{1,2}$  denotes the region overlapped by materials 1 and 2 and  $\bar{\Omega}^{2,3}$  is the region overlapped by materials 2 and 3.

$$\begin{cases} \phi^{s_i}(x) > 0, \forall x \in \Omega^{s_i} \\ \phi^{s_i}(x) = 0, \forall x \in \partial\Omega^{s_i} \\ \phi^{s_i}(x) = 0, \forall x \in D \setminus (\Omega^{s_i} \cup \partial\Omega^{s_i}) \end{cases} \quad (10)$$

where  $\Omega^{s_i} = \bigcup_{j=1}^{n_i} \Omega_j^{s_i}$ ,  $i = 1, 2, \dots, m$  represents the region occupied with the  $i$ -th material (here, the symbol  $n_i$  is the total number of the components made of  $i$ -th material and  $\sum_{i=1}^m n_i = n$ ).  $\phi^{s_i} = \max(\phi_1^{s_i}, \dots, \phi_{n_i}^{s_i})$  denotes the TDF of the  $i$ -th material. As shown in Fig. 2(b), there may be regions overlapped by multiple materials. Thus, the symbol  $\bar{\Omega}$  is introduced to represent these regions in this paper. The property of components in the overlapped areas is the key issue in this study, and a detailed discussion of obtaining the overlapped components' properties will be represented in the next section.

All the design variables can be expressed in a vector form as  $\mathbf{D} = ((\mathbf{D}^1)^\top, \dots, (\mathbf{D}^i)^\top, \dots, (\mathbf{D}^m)^\top)^\top$ , where  $\mathbf{D}^i = ((\mathbf{D}_1^i)^\top, \dots, (\mathbf{D}_j^i)^\top, \dots, (\mathbf{D}_{n_i}^i)^\top)^\top$ . The layout of the  $j$ -th component composed of the  $i$ -th material can be described by the design vector  $\mathbf{D}_j^i$ , where  $\mathbf{D}_j^i = (x_0^{ij}, y_0^{ij}, z_0^{ij}, s_t^{ij}, L^{ij}, h_1^{ij}, h_2^{ij}, h_3^{ij})$  and  $\mathbf{D}_j^i = (x_0^{ij}, y_0^{ij}, z_0^{ij}, s_t^{ij}, s_b^{ij}, s_l^{ij}, L^{ij}, h_1^{ij}, h_2^{ij}, h_3^{ij}, t_1^{ij}, t_2^{ij}, t_3^{ij})$  for 2D and 3D problems, respectively. Based on the previous work [27], the problem formulation of the MMC-based TO method is written as:

$$\begin{aligned} &\text{Find } \mathbf{D} = ((\mathbf{D}^1)^\top, \dots, (\mathbf{D}^i)^\top, \dots, (\mathbf{D}^m)^\top)^\top \\ &\text{Min } I = I(\mathbf{D}) \\ &\text{s.t.} \\ &\quad g_i(\mathbf{D}) \leq 0, \quad i = 1, \dots, m, \\ &\quad \mathbf{D} \in \mathcal{U}_D, \end{aligned} \quad (11)$$

where  $g_i$  is the constraint function of the optimization problem, and  $\mathcal{U}_D$  is the admissible set which  $\mathbf{D}$  belongs to. The classical compliance minimization problem is considered, while the proposed scheme can be easily applied to other design objectives. The constraints are deterministic in our framework, and only the volume fraction constraint of solid material is considered. For universal uncertainties and time-varying design, we refer readers to the work of Wang et al. [56] for details. Linear isotropic materials are used. Finally, the topological design problem with multiple architected materials in our framework can be expressed as:

$$\begin{aligned} &\text{Find } \mathbf{D} = ((\mathbf{D}^1)^\top, \dots, (\mathbf{D}^i)^\top, \dots, (\mathbf{D}^m)^\top)^\top, \\ &\quad \mathbf{u}(x) = ((\mathbf{u}^1)^\top, \dots, (\mathbf{u}^i)^\top, \dots, (\mathbf{u}^m)^\top)^\top \\ &\text{Min } C = \sum_{i=1}^m \int_{\Omega^{s_i}} \mathbf{f}^i \cdot \mathbf{u} dV + \int_{\Gamma_i} \mathbf{t} \cdot \mathbf{u} dS \\ &\text{s.t.} \\ &\quad \sum_{i=1}^m \int_{\Omega^{s_i}} \mathbb{E}^i : \boldsymbol{\varepsilon}(\mathbf{u}^i) : \boldsymbol{\varepsilon}(\boldsymbol{\nu}^i) dV \\ &\quad = \sum_{i=1}^m \int_{\Omega^{s_i}} \mathbf{f}^i \cdot \boldsymbol{\nu}^i dV + \int_{\Gamma_i} \mathbf{t} \cdot \boldsymbol{\nu} dS, \forall \boldsymbol{\nu} \in \mathcal{U}_{ad}, \\ &\quad V_i \leq \bar{V}_i, \\ &\quad \mathbf{D} \in \mathcal{U}_D, \\ &\quad \mathbf{u} = \bar{\mathbf{u}}, \text{ on } \Gamma_u. \end{aligned} \quad (12)$$

In Eq. (12),  $\mathbf{u}$  and  $\boldsymbol{\nu}$  are the displacement field and corresponding test function on  $\mathcal{U}_{ad}$ , where  $\mathcal{U}_{ad} = \{\boldsymbol{\nu} | \boldsymbol{\nu}(x) = \boldsymbol{\nu}^1(x), \forall x \in \Omega^{s_i}; \boldsymbol{\nu}^1 \in H^1(\Omega^{s_i}), \dots, \boldsymbol{\nu}^m \in H^1(\Omega^{s_m}), \text{ and } \boldsymbol{\nu} = 0 \text{ on } \Gamma_u\}$  (here,  $\boldsymbol{\nu}$  is continuous on material interface and  $\Gamma_u$  represents the Dirichlet boundary).  $\bar{\mathbf{u}}$  denotes the prescribed displacement on  $\Gamma_u$  and we take  $\bar{\mathbf{u}} = 0$  for simplicity of calculation. The symbol  $\mathbf{f}^i$  and  $\mathbf{t}$  represent the body force density in  $\Omega^{s_i}$  (the region of the components composed by the  $i$ -th material) and the surface traction on the Neumann boundary  $\Gamma_i$  ( $\mathbf{f}^i = 0$  in the following discussions), respectively.  $\mathbb{E}^i = E^i / (1 + \nu^i) [\mathbb{I} + \nu^i / (1 - 2\nu^i) \boldsymbol{\delta} \otimes \boldsymbol{\delta}]$  ( $\mathbb{I}$  and  $\boldsymbol{\delta}$  denote the symmetric part of the fourth-order identity tensor and second-order identity tensor, respectively) is the fourth-order isotropic elasticity tensor of  $i$ -th material.  $E^i$  and  $\nu^i$  is the corresponding Young's modulus and Poisson's ratio, respectively. The symbol  $\boldsymbol{\varepsilon}$  is the second-order linear strain tensor, and  $\mathcal{U}_D$  is the admissible set that  $\mathbf{D}$  belongs to.  $V_i$  represents the actual volume, and  $\bar{V}_i$  is the upper bound of the available volume in the design domain for  $i$ -th solid material.

## 2.2. Triply periodic minimal surface

In mathematics, a minimal surface is one that has zero mean curvature at each point and has the smallest area that satisfies some constraints. TPMS is an implicit minimum surface period that extends infinitely in three independent directions. A parametric and widely used form to generate TPMSs is to use approximation equations driven from a sum which is defined by Fourier series [57,58]:

$$F(\mathbf{r}) = \sum_k A_k \cos\left(\frac{2\pi \mathbf{h}_k \cdot \mathbf{r}}{\lambda_k} - p_k\right) = C \quad (13)$$

$\mathbf{r}$  is the location vector in Euclidean space,  $A_k$  is the magnitude factor,  $\lambda_k$  is the wavelength of periods,  $\mathbf{h}_k$  represents  $k$ -th lattice vectors in reciprocal space,  $p_k$  is the phase shift, and  $C$  is the iso-surface threshold constant. Gyroid (G), diamond (D), primitive (P), and I-WP surfaces are four typical and commonly-used TPMS types [59], and their

corresponding CAD designs are shown in Fig. 3. A series of level-set equations for these TPMS can be expressed by trigonometric functions [60]:

$$\begin{aligned}
 F^P(x, y, z) &= \cos(x) + \cos(Y) + \cos(Z) - C = 0 \\
 F^G(x, y, z) &= \cos(x)\sin(Y) + \cos(Y)\sin(Z) + \cos(Z)\sin(x) - C = 0 \\
 F^D(x, y, z) &= \sin(x)\sin(Y)\sin(Z) + \sin(x)\cos(Y)\cos(Z) \\
 &\quad + \cos(x)\sin(Y)\cos(Z) + \cos(x)\cos(Y)\sin(Z) - C = 0 \\
 F^{(I-WP)}(x, y, z) &= 2[\cos(x)\cos(Y) + \cos(Y)\cos(Z) + \cos(Z)\cos(x)] \\
 &\quad - [\cos(2X) + \cos(2Y) + \cos(2Z)] - C = 0
 \end{aligned} \tag{14}$$

where  $X = 2\pi x/L_x$ ,  $Y = 2\pi y/L_y$ ,  $Z = 2\pi z/L_z$ ,  $(x, y, z) \in R^3$ ,  $C \in (-1, 1)$ .  $L_x$ ,  $L_y$ ,  $L_z$  are the unit cell sizes in the  $x$ ,  $y$ ,  $z$  directions, respectively.  $C$  ensures the connectivity of the surface and determines the volume fractions within the design regions. Different TPMS has their own beneficial properties. G-surface has a high strength to low filament usage ratio, and P-surface has an advantage in the weight, which could both be used as ultralight materials [61]. The TPMS can be easily controlled by changing the parameters in their implicit function expression to meet different design requirements.

Porous structures based on the TPMSs can be generated in various ways [7,62]. Numerous scaffold designs have driven a paradigm shift from CAD-based approaches to computational modeling methods. In the present work, the implicit functions of TPMS are used to construct the surface model of TPMS. Then, the TPMS surface is offset equidistantly, and the constructed surfaces are closed to obtain a TPMS-based solid structure. The modeling of TPMSs and TPMS-assembled porous structures can be implemented using the software Rhinoceros3D® and Grasshopper® plugin. The volume fraction of a unit cell can be determined by the wall thickness of TPMS-based structures, which is the surface offset.

### 3. Topology optimization with TPMS-infill structure

Based on the formulation of TPMS, an interpolation function is proposed in this section for constructing new porous structures. To establish a connection between the interpolation function and TO, a new ersatz material model is proposed based on the TDF in MMC framework. In the end, the proposed interpolation scheme and the new ersatz material model are used in the multi-material MMC formula.

#### 3.1. The interpolation scheme for TPMS-infill structures

As discussed in the introduction, previous interpolation schemes can neither provide clear transition structures for overlapping components nor model interfacial effects between different materials. To overcome this issue, we use the interpolation schemes in TPMS implicit function expressions. We construct the synthesized TPMSs according to the interpolation TPMS functional expressions, and calculate the mechani-

cal properties of the corresponding porous structures. These synthesized structures can be regarded as the porous materials of the overlapped components. The mechanical properties of the overlapping parts can thus be unambiguous with the distinguishing architecture. The strategy of constructing the implicit function of the TPMSs is expressed as:

$$F = \lambda_1 F_1 + \dots + \lambda_i F_i + \dots + \lambda_m F_m = 0 \tag{15}$$

where symbol  $F_i$  denotes the function of the  $i$ -th TPMS and  $F$  is the implicit function of the composite TPMS.  $\lambda_i$  is the weight coefficient of the  $i$ -th TPMS. The interpolation formula is simple and has been implemented in previous works [63,64]. However, considering that the proposed interpolation method needs to be associated with TO, the selection of weight parameter  $\lambda_i$  becomes the key to connecting the TPMSs expression interpolation with the inverse design. In TO, the proportion of a material (in an element) meets the condition between 0 to 1. Taking the advantage of this characteristic, the volume fraction of the  $i$ -th TPMS in the element is used as the weight value  $\lambda_i$  in the interpolation equation in TO. However, it is worth noting that, when there are more than two kinds of TPMSs in an element, the sum of  $\lambda_i$  may be greater than 1. Thus, a weighted average for  $\lambda_i$  is needed. This weight averaging method will be introduced in the next section. The combination between the proportion of TPMSs and the implicit functions of TPMS can be expressed as:

$$\bar{F}^e = \sum_{i=1}^m \lambda_i^e F_i(x, y, z, C_i) = 0, 0 \leq \lambda_i^e \leq 1, \sum_{i=1}^m \lambda_i^e = 1 \tag{16}$$

where  $\bar{F}^e = \bar{F}^e(x, y, z, C_1, \dots, C_m, \lambda_1, \dots, \lambda_m)$  is the composite implicit function in the  $e$ -th element, and  $\lambda_i^e$  donates to the proportion of  $i$ -th TPMSs in the  $e$ -th element. As introduced in Section 2.2, once the implicit function of the surfaces is obtained, the corresponding solid structure can be directly modeled by CAD software. The effective mechanical properties of the TPMSs are calculated by the homogenization approach. The accuracy of the homogenization method has been tested using the structures with known properties. The resulting maximum error is less than 5% in this work, and this small error does not affect the effectiveness of the design approach. Since many researchers have analyzed the accuracy of homogenization method in multiscale analysis and design problems, we will have no further discussion in this sense but refer readers to [65–67] for detailed descriptions.

In the following analysis of this paper, we take  $C_i = 0$ ,  $i = 1, 2, \dots, m$  [9]. To ensure smoother connectivity between each cell in the optimal result, the wall thickness of the different microstructures needs to be fixed in one optimized design. Some examples of periodic structures composed of P and G surfaces are shown in Fig. 4(a–e). The Young's modulus and Poisson's ratio of different surface structures will be changed with different values of the weight coefficients for different TPMSs. The symbol  $\lambda_G$  is the proportion of G surface in one element, and  $\lambda_P = 1 - \lambda_G$  is the proportion of P surface. Fig. 4(f) represents the equivalent Young's modulus  $\bar{E}$  and Poisson's ratio  $\bar{\nu}$  as a function of the value of  $\lambda_G$ .

In the multi-material TO, the intersection of two TPMSs in the

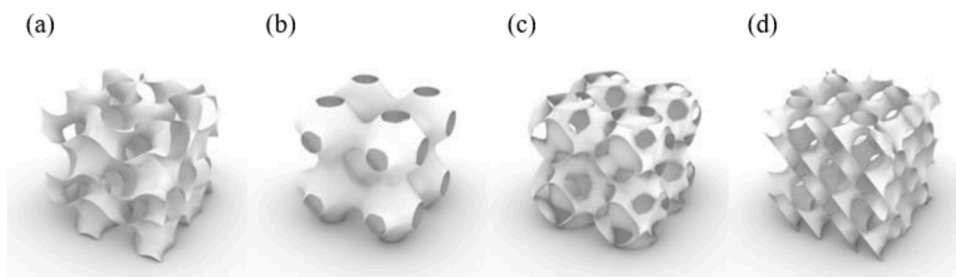
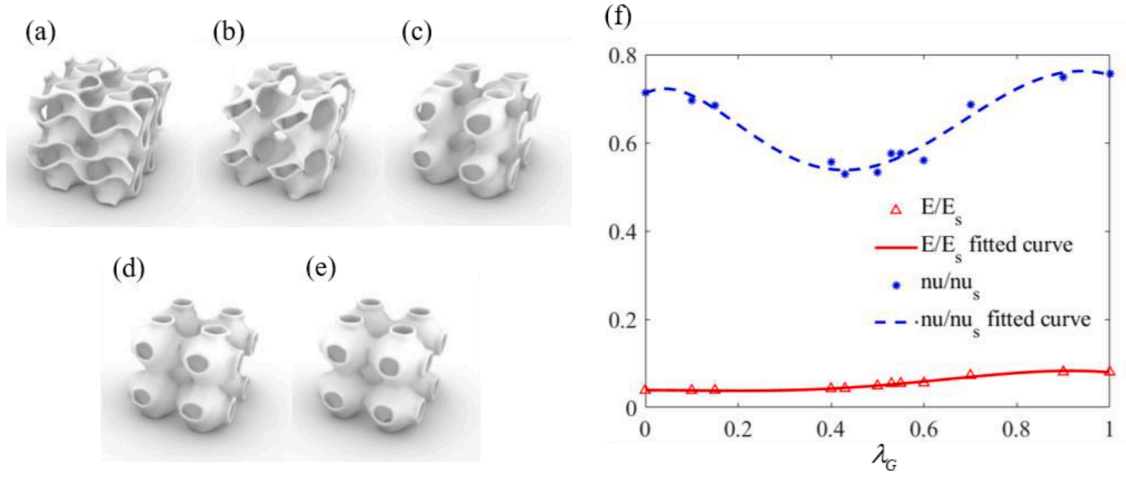


Fig. 3. Four different types of CAD designs of triply periodic minimal surfaces showing  $2 \times 2 \times 2$  tessellation: (a) Gyroid surface; (b) Primitive surface; (c) Diamond surface; (d) I-WP surface.



**Fig. 4.** Composed structures: (a-e) some porous structures composed of Primitive and Gyroid surfaces with different values of  $\lambda_G$ : (a) $\lambda_G = 0.9$ , (b) $\lambda_G = 0.7$ , (c) $\lambda_G = 0.5$ , (d) $\lambda_G = 0.3$ , and (e) $\lambda_G = 0.1$ ; (f) diagram of equivalent mechanical properties as a function of the proportion of G surface  $\lambda_G$ .

optimization structure should have a smooth transition for the sake of easy manufacturing and avoiding stress concentration. A continuous function is thus used here to describe the transition between TPMSs:

$$F_T(x, y, z, C_1, C_2) = \beta(x, y, z)F_1(x, y, z, C_1) + (1 - \beta(x, y, z))F_2(x, y, z, C_2) = 0 \quad (17)$$

where  $\beta$  is the weighting function. According to Yang et al. [63], the Log-Sigmoid function is borrowed to define  $\beta$ :

$$\beta(x, y, z) = \frac{1}{1 + e^{-G(x, y, z)}}, \beta(x, y, z) \in (0, 1) \quad (18)$$

where  $G(x, y, z)$  is a continuous function, and  $G(x, y, z) = 0$  is a spatial coordinate set that describes the boundary between elements. The sectional views showing the connecting location of two different structures are shown in Fig. 5 (here,  $C_1 = 0$ ,  $C_2 = 0$ ,  $G(x, y, z) = x - 5\pi$ ).

### 3.2. Finite element analysis and sensitivity analysis

Since there might be more than one material/architecture infilled in an element for multi-material optimization problems, a new material interpolation approach has been proposed in the previous section to interpolate the implicit functions of TPMS to generate new architectures. In this scheme, the property of the TPMS-architected materials is related to the weight coefficient of the TPMS, which will in turn influence the mechanical property of the assembled structure. The MMC-based TO, like most TO methods, use the strategy of uniformly dividing the design domain into finite elements. According to Zhang et al. [54], the ersatz material model is also adopted here to improve the efficiency of finite element analysis. Therefore, a connection is

established between the mechanical properties (i.e., Young's modulus and Poisson's ratio) of the infill structures and the TDF value of the node of the element, and this connection should be also related to the proposed interpolation scheme to combine the interpolation expression of TPMS implicit function with TO.

$$E^e(\rho_1^e, \dots, \rho_m^e) = \rho^e \bar{E} \quad (19)$$

In Eq. (19),  $E^e$  denotes the Young's modulus of  $e$ -th element, and  $\rho^e = \sum_{i=1}^m \rho_i^e$  is the volume fraction of solid materials in  $i$ -th element. The symbol  $\rho_i^e$  denotes the infill rate of  $i$ -th material.  $\bar{E} = \bar{E}(\lambda_1^e, \dots, \lambda_i^e, \dots, \lambda_m^e)$  is the equivalent Young's modulus of porous structures.  $\lambda_i^e$  represents the proportion of material  $i$  in the  $e$ -th element, which can be written as:

$$\lambda_i^e = \frac{\rho_i^e}{\sum_{j=1}^m \rho_j^e}, i = 1, 2, \dots, m, \quad (20)$$

It is worth noting that there may be a node of the element that is overlapped by multiple materials. If this circumstance is ignored, the value of solid materials infill rate  $\rho^e$  is likely to be greater than 2, which is infeasible. To solve this problem, a parameter  $\omega_i^{ek}$  is introduced here acting as the weight coefficient of Heaviside function on the  $k$ -th node of the  $e$ -th element. The values of  $\rho_i^e$  for 2D and 3D problems can be expressed as:

$$\rho_i^e = \frac{1}{4} \sum_{k=1}^4 \omega_i^{ek} H(\phi_i^{ek}) \quad (21)$$

and

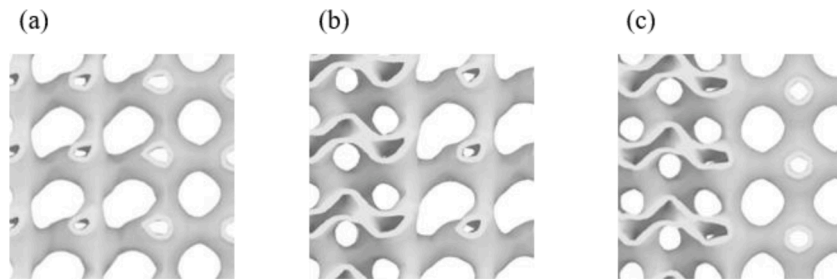


**Fig. 5.** Planar view of the transition of different structures: (a) from porous structure with  $\lambda_p = 0.5, \lambda_G = 0.5$  to porous structure with  $\lambda_p = 0.9, \lambda_G = 0.1$  (from left to right); (b) from porous structure with  $\lambda_p = 0.1, \lambda_G = 0.9$  to porous structure with  $\lambda_p = 0.5, \lambda_G = 0.5$ ; (c) from porous structure with  $\lambda_p = 0, \lambda_G = 1$  to porous structure with  $\lambda_p = 1, \lambda_G = 0$ .

$$\rho_i^e = \frac{1}{8} \sum_{k=1}^8 \omega_i^{ek} H(\phi_i^{ek}) \quad (22)$$

with

$$\omega_i^{ek} = \begin{cases} \frac{1}{N}, & \text{if } \phi_i^{ek} \geq 0, \\ 1, & \text{otherwise} \end{cases} \quad (23)$$

where  $\phi_i^{ek}$  is the TDF value of the  $i$ -th material for the  $k$ -th node of the  $e$ -th element. In Eq. (23), the symbol  $N$  represents the number of materials occupying the  $k$ -th node of the element  $e$ .  $H = H(x)$  is the Heaviside function. In order to better explain the operation of the proposed interpolation scheme, Fig. 6 shows some examples for the above interpolation scheme. The TDF values of the two materials on the nodes of element 2 are obtained in Fig. 6(c), and they can be brought to Eq. (23) for the weight coefficient  $\omega_1^{2,k}$  and  $\omega_2^{2,k}$  ( $k$  is the node number). Next,  $\rho_1^2$  and  $\rho_2^2$  can be calculated by Eq. (21). We then can bring the  $\rho_1^2$  and  $\rho_2^2$  to Eq. (20) to get  $\lambda_1^2 = 0.75$  and  $\lambda_2^2 = 0.25$ . Since the properties of the two materials are accessed, the implicit function expression and Young's modulus of the microstructure in element 2 can be obtained according to Eq. (16) and the fitted function mentioned in Section 3.1. For the stability of optimization, the expression of the Heaviside function is

replaced by its regularized version  $H_\epsilon(x)$ :

$$H_\epsilon(x) = \begin{cases} 1, & \text{if } x > \epsilon, \\ \frac{3(1-\alpha)}{4} \left( \frac{x}{\epsilon} - \frac{x^3}{3\epsilon^3} \right) + \frac{1+\alpha}{2}, & \text{if } -\epsilon < x < \epsilon, \\ \alpha, & \text{otherwise} \end{cases} \quad (24)$$

In Eq. (24), the symbol  $\epsilon$  is the parameter adopted for the magnitude of regularization, and  $\alpha$  is a relatively small positive number to ensure that the stiffness matrix is nonsingular. This paper only gives the calculation of Young's modulus since the way of the calculation of the Poisson's ratio  $\nu^e$  is the same. Based on the discussion mentioned above, the stiffness matrix of the  $e$ -th element is expressed as:

$$\mathbf{k}^e = \int_{\Omega_e} \mathbf{B}^T \mathbf{D}^e \mathbf{B} dV \quad (25)$$

where  $\Omega_e$  is the region occupied by the  $e$ -th element, and  $\mathbf{B}$  is the strain matrix.  $\mathbf{D}^e$  denotes the elasticity matrix of the  $e$ -th element (here,  $\mathbf{D}^e = \rho^e \bar{\mathbf{D}}$ ,  $\bar{\mathbf{D}}$  is the elasticity matrix of the porous structure).

Consequently, the derivative of the objective of compliance and the volume constraint with respect to the parameter  $\alpha$  for 2D problems can be expressed as:

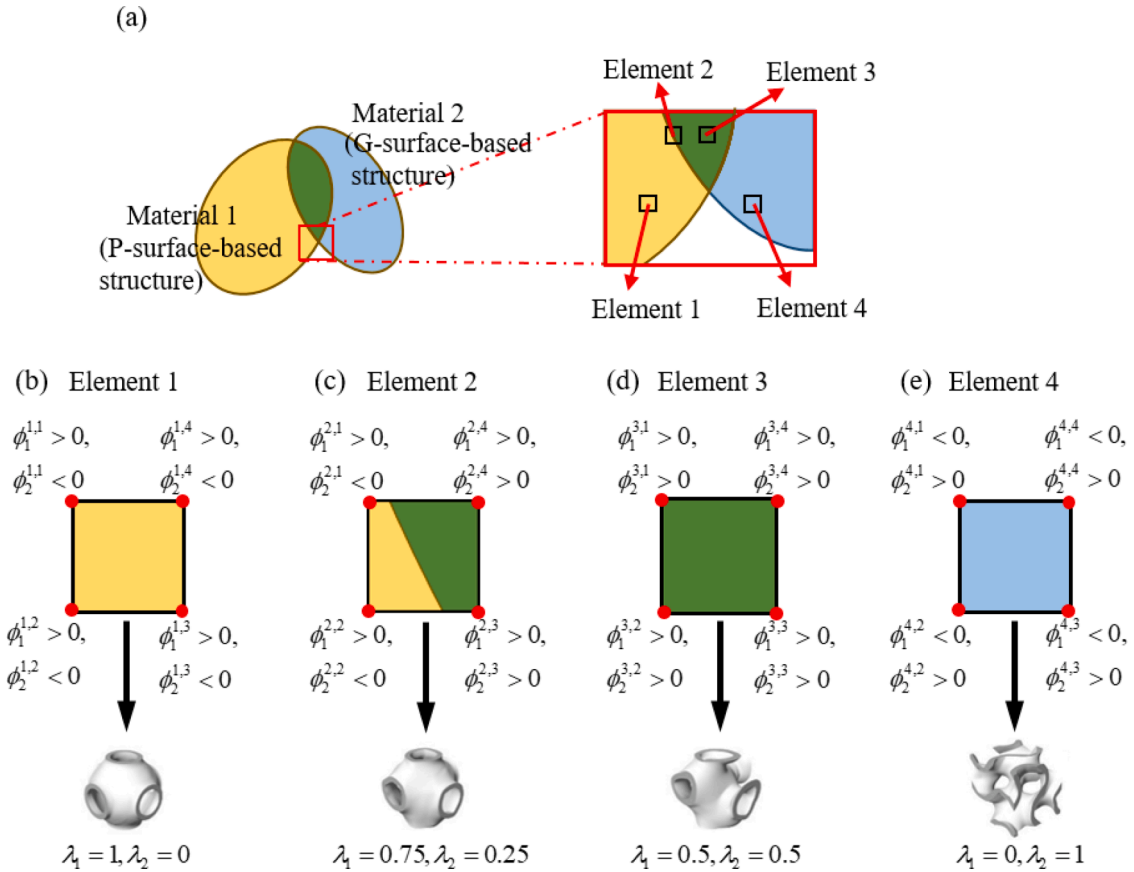


**Fig. 6.** A schematic illustration of the proposed interpolation scheme: (a) intersection of two components infilled with different materials. The color yellow and blue represent the regions infilled with materials 1 and 2, respectively, and the green region denotes the domain overlapped by the two materials; (b-e) some examples about the distribution of materials and the corresponding infill morphology in one element.  $\phi$  is the TDF value of the material on the node, e.g.  $\phi_1^{2,3}$  is the TDF value of material 1 on the 3rd node of element 2.

$$\begin{aligned}
\frac{\partial C}{\partial \alpha} &= -\mathbf{u}^\top \frac{\partial \mathbf{K}}{\partial \alpha} \mathbf{u} \\
&= -\mathbf{u}^\top \left( \sum_{e=1}^{NE} \frac{\partial \mathbf{k}^e}{\partial \alpha} \right) \mathbf{u} \\
&= -\mathbf{u}^\top \left( \sum_{e=1}^{NE} \sum_{i=1}^m \frac{\partial \mathbf{k}^e}{\partial \rho_i^e} \frac{\partial \rho_i^e}{\partial \alpha} \right) \mathbf{u} \\
&= -\mathbf{u}^\top \left( \sum_{e=1}^{NE} \sum_{i=1}^m \left( \frac{\partial \mathbf{k}^e}{\partial E^e} \frac{\partial E^e}{\partial \rho_i^e} + \frac{\partial \mathbf{k}^e}{\partial \nu^e} \frac{\partial \nu^e}{\partial \rho_i^e} \right) \frac{\partial \rho_i^e}{\partial \alpha} \right) \mathbf{u} \\
&= -\mathbf{u}^\top \left( \frac{1}{4} \sum_{e=1}^{NE} \sum_{i=1}^m \left( \frac{\partial \mathbf{k}^e}{\partial E^e} \frac{\partial E^e}{\partial \rho_i^e} + \frac{\partial \mathbf{k}^e}{\partial \nu^e} \frac{\partial \nu^e}{\partial \rho_i^e} \right) \sum_{k=1}^4 \omega_i^{ek} \frac{\partial H_e(\phi_i^{ek})}{\partial \alpha} \right) \mathbf{u}
\end{aligned} \tag{26}$$

and

$$\frac{\partial V_i}{\partial \alpha} = \frac{1}{4} \sum_{e=1}^{NE} \sum_{k=1}^4 \omega_i^{ek} \frac{\partial H_e(\phi_i^{ek})}{\partial \alpha} \tag{27}$$

respectively. In Eq. (26),  $\mathbf{K}$  is the global stiffness matrix, and  $\mathbf{k}^e$  is the element stiffness matrix.  $NE$  is the total number of elements in the design domain. In this work,  $\frac{\partial H_e(\phi_i^{ek})}{\partial \alpha}$  is calculated using the direct partial derivative method. The sensitivity analysis for 3D problems can be calculated similarly. During the optimization, the method of moving asymptotes (MMA) is used to update the design variable. A flow chart of implementing the proposed framework is given in Fig. 7.

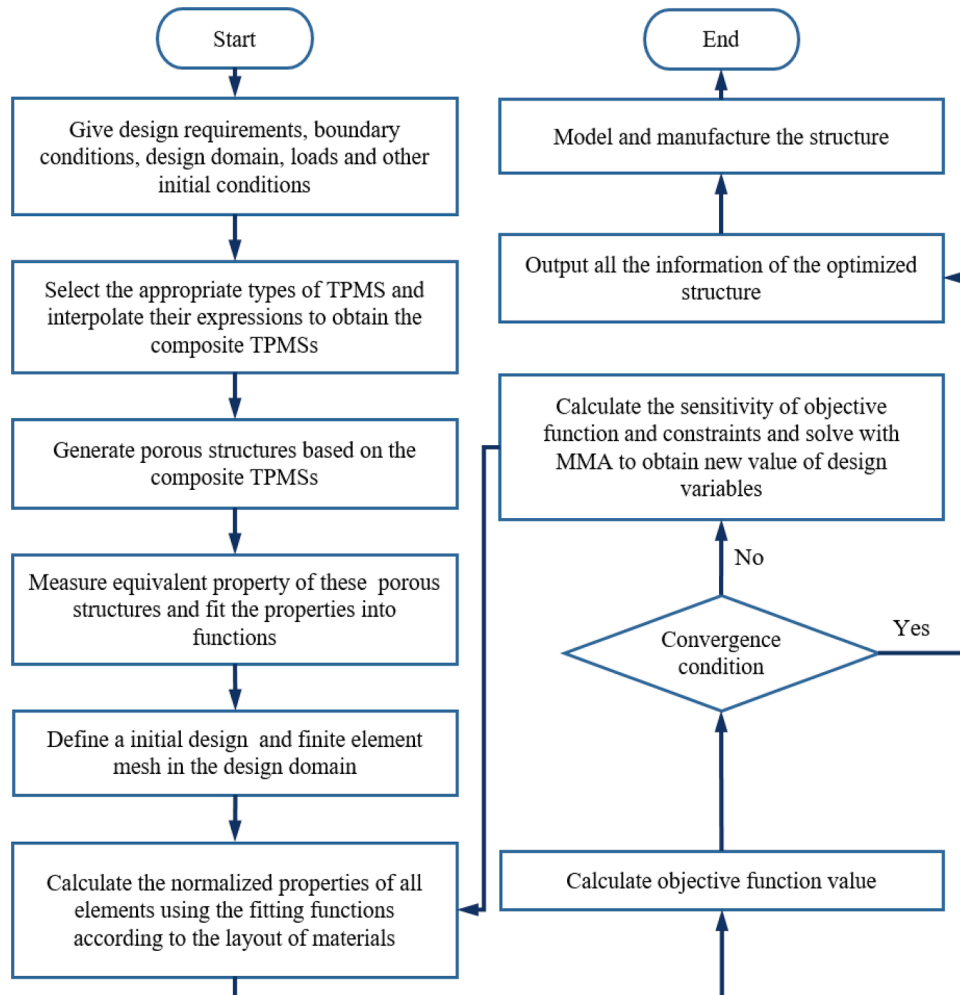


Fig. 7. Flow chart of implementing the proposed design approach.

#### 4. Numerical examples

In this section, some numerical examples are presented to illustrate the effectiveness and efficiency of the proposed method. All the examples here are minimizing the structural compliance within a given volume constraint. In the following examples, for simplicity, the effect of gravity is not considered and all the quantities are dimensionless. The initial material phases are selected as three: two solid materials (i.e., P-surface-based structure and G-surface-based structure) and one void material. The design domain is discretized with 4-node quadrilateral elements for 2D problems and 8-node hexahedron elements for 3D problems. In the following discussion, material 1 and material 2 are used to represent P-surface-based structure and G-surface-based structure separately for the convenience of description. The corresponding Young's moduli and Poisson's ratios are  $E_1 = 4.24$ ,  $\nu_1 = 0.217$  and  $E_2 = 8.00$ ,  $\nu_2 = 0.227$ , respectively. It is worth noting that, the mechanical properties of the two materials above are approximated by the homogenization method in Section 3.1. The TPMSs microstructure is modeled in Rhinoceros3D® software. The process of multi-material TO is then implemented in MATLAB®.

##### 4.1. 2D examples

This subsection shows several 2D examples to illustrate the performance of the proposed TO method and presents the difference in optimized results when given conditions of the optimization problem are changed. Note that components with a particularly small volume will be

removed through filtering.

#### 4.1.1. Two-bar beam example

The classic two-bar beam problem is taken into consideration first. The boundary condition for this example is depicted in Fig. 8(a). The left side is fixed, and a downward concentrated load is applied at the middle of the right edge. The design domain is assumed to be a  $1 \times 2$  rectangle area with a unit thickness and discretized with a square mesh  $60 \times 120$ . We first consider an initial design with the component layout as Fig. 8 (b), where there are 12 components in the design domain, including 6 components composed of material 1 and the rest made of material 2. Each component has the same shape and size, while the central coordination and the angle of inclination are different. The volume fraction for the two materials is limited as  $V_1/V_D = 0.15$  and  $V_2/V_D = 0.05$ . Fig. 8 (c) depicts the component plot of the optimized structure. The result is similar to results acquired by other TO approaches. Material 1 mainly distributes at the boundary and the node where the load is fixed. Material 2 constitutes the load transmission path.

Three cases are used to show the influence of the initial design. The volume constraints of all the cases are the same as the previous one. The given initial designs and corresponding results are shown in Fig. 9. The numbers of components consisting of material 1 and material 2 are the same for the first two cases in Fig. 9. Both of the first two cases have 12 components in the initial design domain. In the first case here, the components composed of both materials are completely overlapped. In the third case, there are 4 initial components composed of material 1 and two composed of material 2. It is seen that final material layouts in these cases are similar and the maximum difference in the objective functions is less than 2.5%.

#### 4.1.2. Short beam example

The design domain for a 2D short cantilever is plotted in Fig. 10(a). The initial design domain is discretized using a mesh of  $160 \times 80$  finite elements with a unit thickness. The displacement of the left side is set to zero, and a vertical load is applied on the middle point of the right side.

Firstly, four cases are studied here to show how the different volume constraints of the two materials will affect the optimized topology. The initial designs for these cases are the same, as shown in Fig. 10(b). There are 16 components in the design domain divided equally between the two materials. Material 1 and Material 2 overlap each other so only the

cyan color is represented in Fig. 10(b). The different volume distributions and corresponding results are plotted in Fig. 10(c-f).

To illustrate the optimization process, the case of Fig. 10(c) is taken as an example here. Fig. 11(a-d) presents structures for intermediate iteration steps during optimization. The difference in the objective function values for this case is also compared with optimization using only a single material. The iteration history of the objective function is shown in Fig. 11(e), including two single-material cases and one multi-material case. The three cases have the same initial design and the volume fraction constraint of the two single-material cases is set as  $V/V_D=0.4$ . The objective function values in this example tend to be stable after 100 iterations. The final value for the multi-material case is between the two single-material cases, which is foreseeable for multi-material TO problem.

The following example is about different initial designs for the case of  $V_1/V_D=0.3, V_2/V_D=0.1$ . The initial designs and corresponding results are demonstrated in Fig. 12. The optimized structures will be similar only if their initial designs have similar material and component distributions. The emergence of this situation is predictable and inevitable since the problem is nonconvex in nature. Although the optimized structures are different, the objective function values have only a slight change.

#### 4.2. 3D example

In this subsection, the performance of the proposed approach for a 3D problem is examined. The design domain of the 3D problem is chosen as a cuboid region of  $8 \times 0.4 \times 4$  as plotted in Fig. 13(a). The left side of the design domain is fixed and there is a vertical load at the center point of the right side. The computations in this example are performed with  $80 \times 4 \times 40$  eight-node cubic elements. There are 16 components in the design domain, and the initial layout and shape of the components are shown in Fig. 13(b). The maximum volume fraction is given as  $V_1/V_D=0.2, V_2/V_D=0.1$  for the two materials, respectively. The optimal topology for this case is shown in Fig. 13(c). Material 2 occupies the right boundary of the path that transmits the external load and material 1 is shown on the left side, while the two materials alternate in the middle of the track. Meanwhile, material 1 also constitutes an X-like structure to support the path and transmit the shear force.

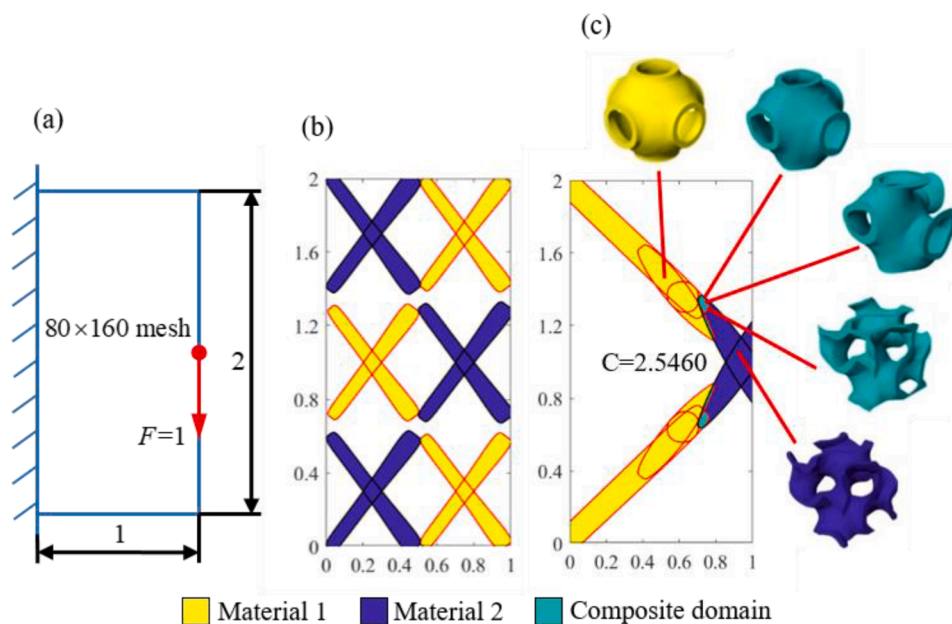


Fig. 8. Two-bar example: (a) design domain, external load, and boundary conditions; (b) initial design; (c) the optimized result and the unit models of material 1, material 2, and partial composed structures.

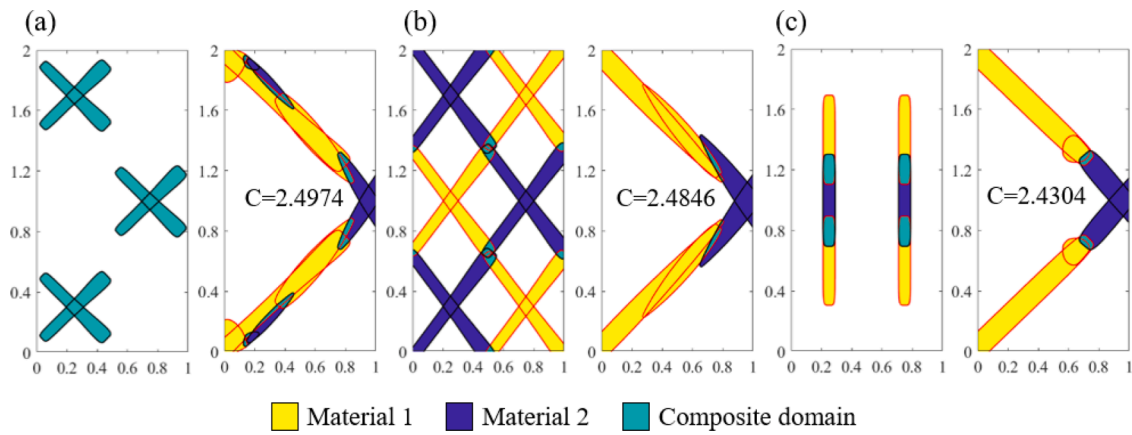


Fig. 9. Optimized topologies with different initial designs for the two-bar example: (a-c) three different cases, including the initial design (the left figure in each case) and corresponding optimal result (the right figure in each case), respectively.

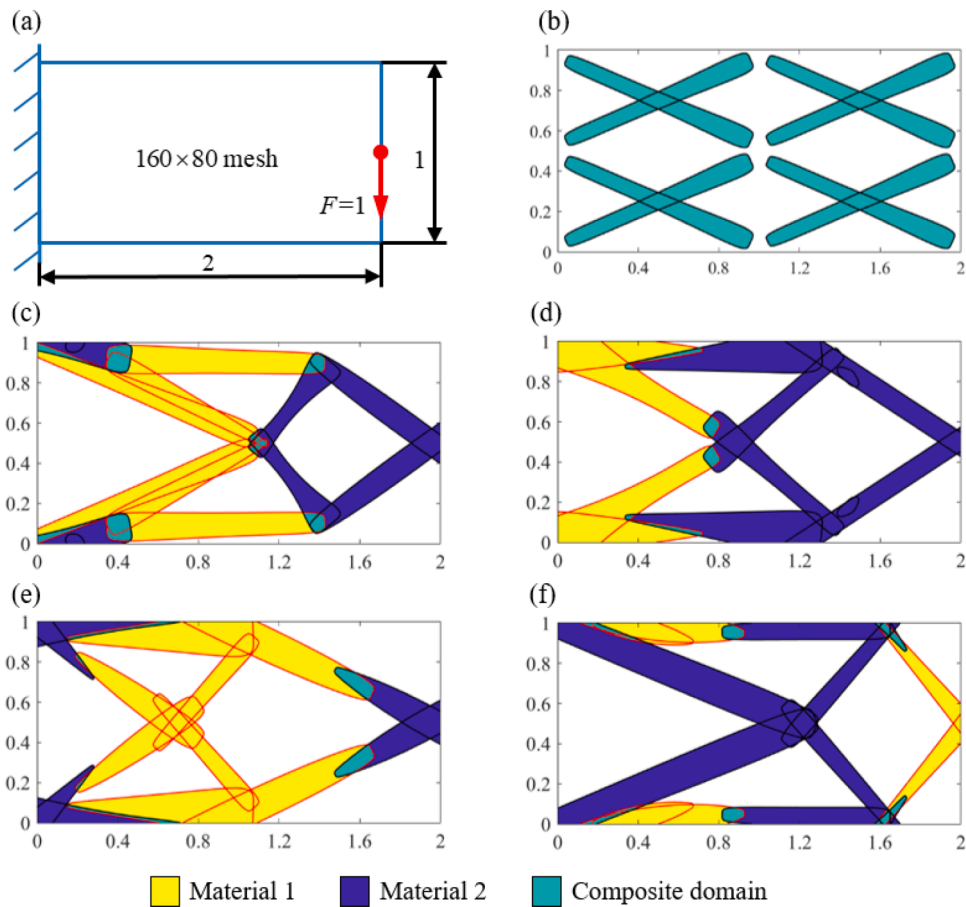


Fig. 10. The 2D short beam: (a) 2D design domain and boundary condition; (b) initial 2D design; (c-f) optimized topology under different volume constraints for the two materials: (c)  $V_1/V_D=0.25, V_2/V_D=0.15$ , (d)  $V_1/V_D=0.15, V_2/V_D=0.25$ , (e)  $V_1/V_D=0.3, V_2/V_D=0.1$ , and (f)  $V_1/V_D=0.1, V_2/V_D=0.3$ .

### 4.3. Analysis and manufacture of the optimized result

When using minimal surfaces as infill materials in traditional multi-material TO, one point to consider is how the components composed of different minimal surfaces are connected when manufacturing the solid model of the optimization result. In some cases, these constructions may not be connected, or the connection may result in poor simulation performance. These situations can have an impact on the performance of the optimization results. In the proposed TO approach, the optimization results in multiple microstructures for transition in the region where the

components of different TPMS are connected. To illustrate the advantages of material transitions in the optimization results obtained by this approach, an optimized model with transition structures and a model with direct connections are generated. These solid models are constructed based on the case for Fig. 8(c). Structural analysis is performed for both models according to the boundary conditions of Fig. 8(a), and the obtained von Mises stress contributions are shown in Fig. 14 (a,b). The models here are constructed in Rhinoceros3D® and analysis is implemented in SimSolid®. It can be easily observed that the stress concentration at the junction of two TPMSs has been significantly

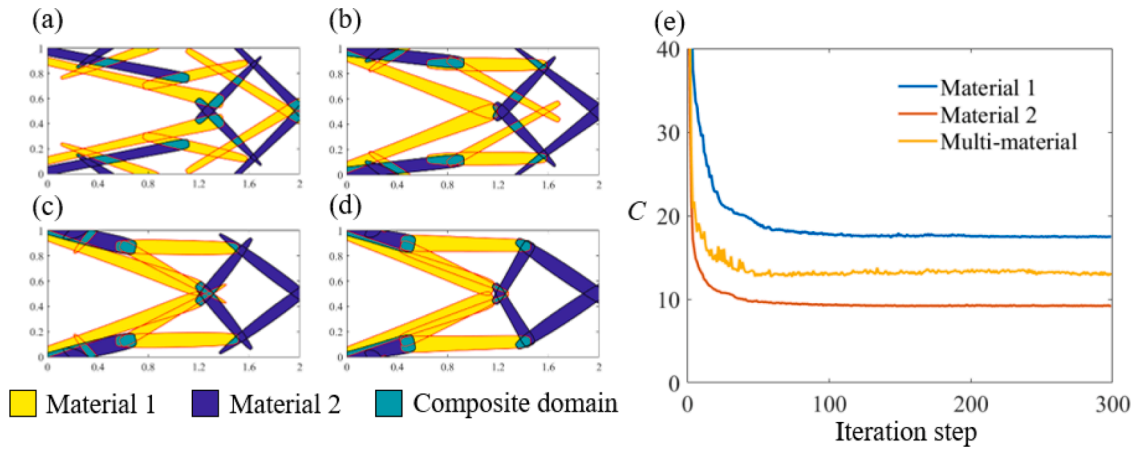


Fig. 11. Example for the case of Fig. 10(c): (a-d) four topologies in different intermediate steps: (a) Step 11, (b) Step 46, (c) Step 84, and (d) Step 255; (e) diagram of the iteration history of objective function value for single-material and multi-material cases.

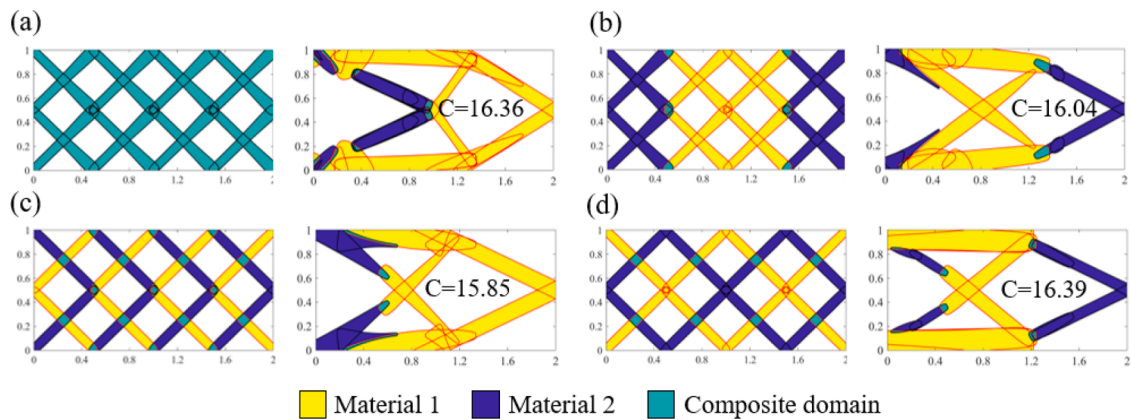


Fig. 12. The optimized topologies with different initial designs for short beam example: (a-d) four different cases. In each case, the left figure demonstrates the initial design and the right figure shows the material distribution of the optimized result. The volume constraint of the two materials in (a-d) is  $V_1/V_D=0.3, V_2/V_D=0.1$ .

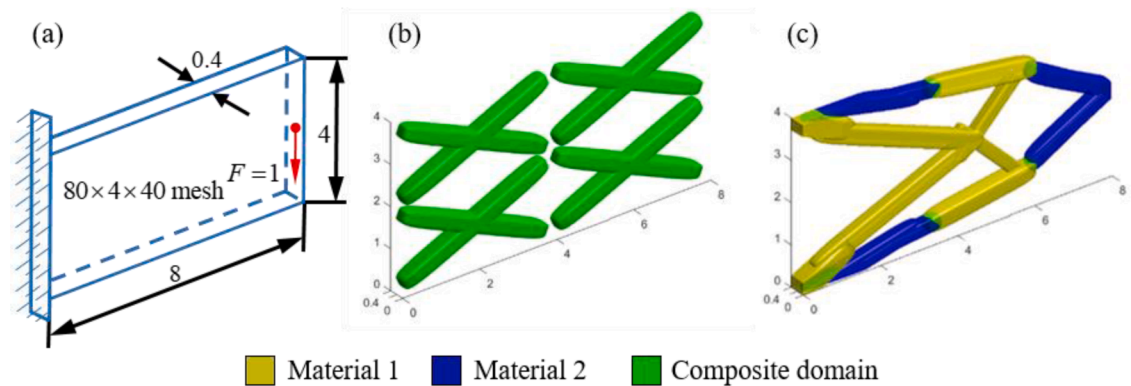
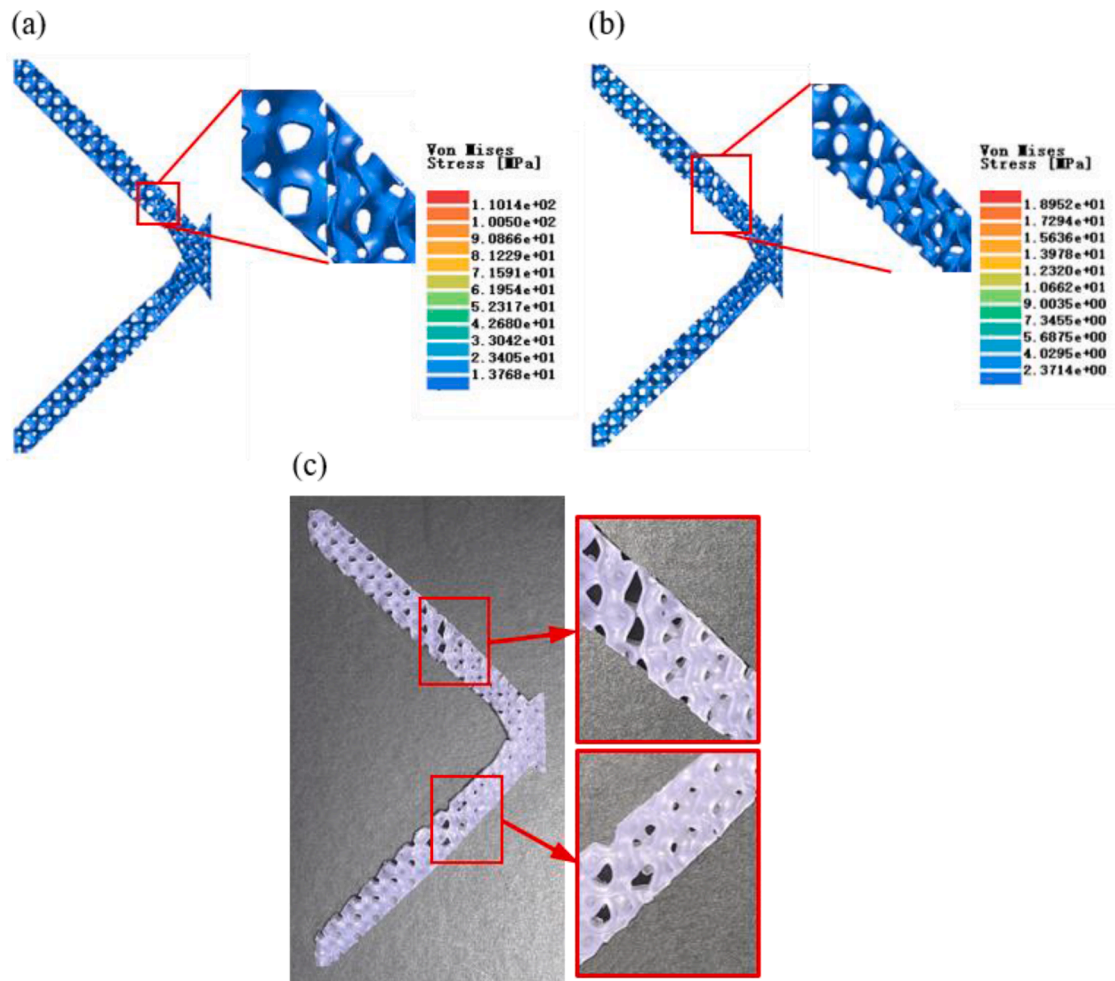


Fig. 13. The 3D cantilever beam: (a) 3D design domain; (b) initial 3D design; (c) the optimized structure with designed distribution of different involved materials, where the volume constraint is  $V_1/V_D=0.2, V_2/V_D=0.1$ .

reduced in the model with transition comparing to the model without transition. This illustrates that the geometric model obtained by the proposed approach has more suitable internal structures and thus fewer errors caused by the equivalent property in TO. It is worth noting that, to make the microstructures inside the model more observable, a relatively coarser mesh is chosen during the modeling and simulation of the optimized structure, and the number of TPMS microstructures will be decreased correspondingly. Although this reduction will lose some

accuracy, it would be efficient to quantify the significance of our method compared with the old ones.

The constructed multi-microstructure model is printed by a 3D printer (Formlabs Form2 SLA 3D printer) to present the manufacturability. The printed model is shown in Fig. 14(c), from which explicit microstructures of overlapping components can be seen, verifying the manufacturing feasibility of the proposed TO approach.



**Fig. 14.** The optimized result of the case for Fig. 8(c): (a) the model without transition and the corresponding von Mises stress distribution; (b) the model with multiple microstructures (for transition) and its von Mises stress distribution; (c) the 3D printed physical structure.

#### 4.4. Practical engineering design for the automotive connecting rod

To demonstrate the application of the proposed approach in engineering, the automotive connecting rod is taken as an example in this section. For calculation and presentation purposes, the boundary conditions are simplified and the connecting rod is subjected only to compression load, as shown in Fig. 15 (a). The two pin holes of the large end are fixed in every direction. The design domain is framed in blue. In this example, the maximum volume ratios of two materials are  $V_1/V = 0.65$ ,  $V_2/V = 0.35$ , respectively. The initial design is shown in Fig. 15(b). There are 12 components in the design domain and 6 of them are made of material 1. The shapes and sizes of all the components are the same. The components infilled with material 2 are overlapped with components made of material 1.

This example is implemented by using both MATLAB® and ANSYS®. Materials distributions of the optimized result and finite element node information in ANSYS® are exported to CAD software to generate the porous structure model. The optimized rod is presented in Fig. 15(c), and the corresponding objective value (structural compliance) of the result is  $2.26 \times 10^4$ . Some infill microstructures are amplified in Fig. 15 (b-c). In Fig. 15(c), the edges of the components infilled with material 1 are shown in red lines and those of material 2 are marked by blue lines.

## 5. Conclusions

How to deal with interfacial domain is a challenging topic in engineering design involving multiple materials. Existing works often

neglect this challenge or cannot provide a meaningful transition with physical characteristics. This work, by introducing a new function-based material interpolation scheme, provides an efficient way to conduct multi-scale and multi-material structural design considering the interfacial domain. The specific TMPS architected material serves as the infill structure at the lower scale of design, while the overall distribution of infill structures is achieved by TO.

The parameterized representation of TMPS-based porous structures makes the structures can be directly combined with TO. A set of level set functions are used to identify the interpolation parameters that determine the TMPS with accurate material characteristics. Therefore, the structural morphology and corresponding properties of infill microstructures can be obtained in terms of the interpolation parameters, which provides the accurate structural representation of the multi-material overlapped regions. In addition, the MMC-based topology optimization further reduces the design variable and provides explicit geometric representations.

Both 2D and 3D numerical examples are tested to demonstrate that the proposed method successfully generates smooth transitions between different TMPSs during the TO, and the smooth transitions overcome the microstructural mismatch in conventional methods and significantly reduce the stress concentration. An automotive connecting rod further demonstrates the effectiveness of the proposed method in practical engineering problems.

The proposed TO method is not limited to infilling TPMS-based microstructures or solving minimum compliance problems. Other physics and constraints can be also incorporated into this engineering design

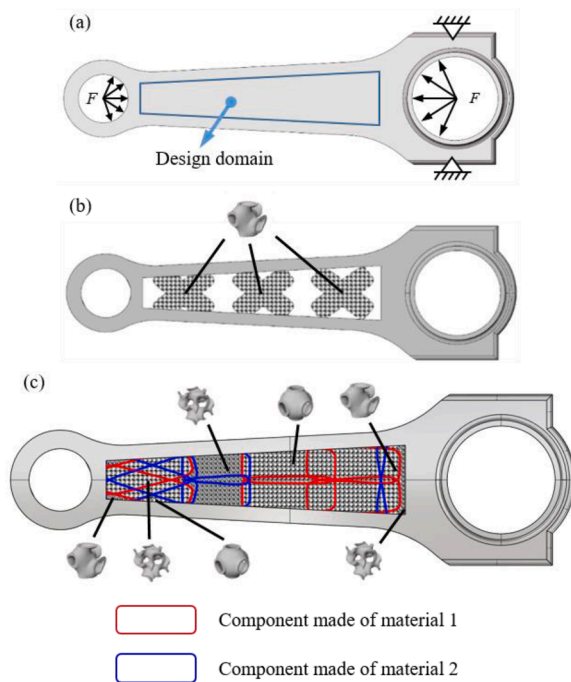


**Fig. 15.** Design for the automotive connecting rod: (a) the boundary conditions and design domain of the automotive connecting rod; (b) the structural model of the initial design and the infill morphology; (c) the structural model of the optimized result and some infill microstructures in the models. The boundaries of components are represented by different colors: components infilled with material 1 are marked by red and those infilled with material 2 are in blue color.

framework as interesting future works.

#### CRediT authorship contribution statement

**Sinuo Zhang:** Methodology, Investigation, Data curation, Writing – original draft. **Daicong Da:** Supervision, Writing – review & editing. **Yingjun Wang:** Conceptualization, Supervision, Writing – review & editing.

#### Declaration of Competing Interest

The authors declare that they have no known competing financial interests or personal relationships that could have appeared to influence the work reported in this paper.

#### Data availability

Data will be made available on request.

#### Acknowledgment

This work has been supported by National Natural Science Foundation of China [No. 52075184], Guangdong Basic and Applied Basic Research Foundation (2019A1515011783), Open-funding Project of State Key Laboratory of Digital Manufacturing Equipment and Technology (Huazhong University of Science and Technology) [No. DMETKF2021020]. These supports are gratefully acknowledged.

#### References

- [1] Almshergqi Z, Margadant F, Deng YR. A look through 'lens' cubic mitochondria. *Interface Focus* 2012;2:539–45.
- [2] Almshergqi ZA, Landh T, Kohlwein SD, Deng YR. Cubic membranes: the missing dimension of cell membrane organization. *Int Rev Cell Mol Biol* 2009;274:275–342.
- [3] Michielsen K, Stavenga DG. Gyroid cuticular structures in butterfly wing scales: biological photonic crystals. *J R Soc, Interface* 2008;5:85–94.
- [4] Groen JP, Sigmund O. Homogenization-based topology optimization for high-resolution manufacturable microstructures. *Int J Numer Methods Eng* 2018;113:1148–63.
- [5] Wang J, Chen WW, Da DC, Fuge M, Rai R. IH-GAN: A conditional generative model for implicit surface-based inverse design of cellular structures. *Comput Meth Appl Mech Eng* 2022;396:115060.
- [6] Yoo D-J. Advanced porous scaffold design using multi-void triply periodic minimal surface models with high surface area to volume ratios. *Int J Precis Eng Manuf* 2014;15:1657–66.
- [7] Kapfer SC, Hyde ST, Mecke K, Arns CH, Schröder-Turk GE. Minimal surface scaffold designs for tissue engineering. *Biomaterials* 2011;32:6875–82.
- [8] Aremu A, Maskery I, Tuck C, Ashcroft I, Wildman R, Hague R. A comparative finite element study of cubic unit cells for selective laser melting. In: 2014 International Solid Freeform Fabrication Symposium. University of Texas at Austin; 2014.
- [9] Maskery I, Sturm L, Aremu AO, Panesar A, Williams CB, Tuck CJ, Wildman RD, Ashcroft IA, Hague RJ. Insights into the mechanical properties of several triply periodic minimal surface lattice structures made by polymer additive manufacturing. *Polymer* 2018;152:62–71.
- [10] Jung Y, Torquato S. Fluid permeabilities of triply periodic minimal surfaces. *Phys Rev E* 2005;72:056319.
- [11] Bendsoe MP, Kikuchi N. Generating optimal topologies in structural design using a homogenization method. *Comput Meth Appl Mech Eng* 1988;71:197–224.
- [12] Bendsoe MP, Sigmund O. Material interpolation schemes in topology optimization. *Arch Appl Mech* 1999;69:635–54.
- [13] Zhou M, Rozvany G. The COC algorithm. Part II: Topological, geometry and generalised shape optimisation. *Comput Methods Appl Mech Eng*. 9 1991;191:224.
- [14] Mei YL, Wang XM. A level set method for structural topology optimization and its applications. *Adv Eng Softw* 2004;35:415–41.
- [15] Wang MY, Wang XM, Guo DM. A level set method for structural topology optimization. *Comput Meth Appl Mech Eng* 2003;192:227–46.
- [16] Xie YM, Steven GP. A simple evolutionary procedure for structural optimization. *Comput Struct* 1993;49:885–96.
- [17] Huang XD, Xie YM. Bi-directional evolutionary topology optimization of continuum structures with one or multiple materials. *Comput Mech* 2009;43:393–401.
- [18] Da DC, Xia L, Li GY, Huang XD. Evolutionary topology optimization of continuum structures with smooth boundary representation. *Struct Multidiscip Optim* 2018;57:2143–59.
- [19] Wang YJ, Benson DJ. Isogeometric analysis for parameterized LSM-based structural topology optimization. *Comput Mech* 2016;57:19–35.
- [20] Wang YJ, Liao ZY, Ye M, Zhang Y, Li WH, Xia ZH. An efficient isogeometric topology optimization using multilevel mesh, MGCG and local-update strategy. *Adv Eng Software* 2020;139:102733.
- [21] Wang C, Zhao Z, Zhou M, Sigmund O, Zhang XS. A comprehensive review of educational articles on structural and multidisciplinary optimization. *Struct Multidiscip Optim* 2021;64:2827–80.
- [22] Da DC. Model reduction on 3D fracture resistance design. *J Comput Phys* 2022;463:111274.
- [23] Dirker J, Meyer JP. Topology optimization for an internal heat-conduction cooling scheme in a square domain for high heat flux applications. *J Heat Transf* 2013;135.
- [24] Lindgaard E, Dahl J. On compliance and buckling objective functions in topology optimization of snap-through problems. *Struct Multidiscip Optim* 2013;47:409–21.
- [25] Nørgaard S, Sigmund O, Lazarov B. Topology optimization of unsteady flow problems using the lattice Boltzmann method. *J Comput Phys* 2016;307:291–307.
- [26] Zheng YF, Wang YJ, Lu X, Liao ZY, Qu JP. Evolutionary topology optimization for mechanical metamaterials with auxetic property. *Int J Mech Sci* 2020;179:105638.
- [27] Guo X, Zhang WS, Zhong WL. Doing topology optimization explicitly and geometrically—a new moving morphable components based framework. *J Appl Mech* 2014;81.
- [28] Guo X, Zhang WS, Zhang J. Explicit structural topology optimization based on morphable components with complex shapes, in, submission, 2015.
- [29] Zhang WS, Song JF, Zhou JH, Du ZL, Zhu YC, Sun Z, Guo X. Topology optimization with multiple materials via moving morphable component (MMC) method. *Int J Numer Methods Eng* 2018;113:1653–75.
- [30] Xie XD, Wang ST, Xu MM, Wang YJ. A new isogeometric topology optimization using moving morphable components based on R-functions and collocation schemes. *Comput Meth Appl Mech Eng* 2018;339:61–90.
- [31] Liu C, Zhu YC, Sun Z, Li DD, Du ZL, Zhang WS, Guo X. An efficient moving morphable component (MMC)-based approach for multi-resolution topology optimization. *Struct Multidiscip Optim* 2018;58:2455–79.
- [32] Li DZ, Kim IY. Multi-material topology optimization for practical lightweight design. *Struct Multidiscip Optim* 2018;58:1081–94.
- [33] Li C, Kim IY. Multi-material topology optimization for automotive design problems. In: Proceedings of the institution of mechanical engineers, Part D: journal of automobile engineering. 232; 2018. p. 1950–69.
- [34] Da DC, Yvonnet J, Xia L, Li GY. Topology optimization of particle-matrix composites for optimal fracture resistance taking into account interfacial damage. *Int J Numer Methods Eng* 2018;115:604–26.
- [35] Dunning P, Kim HA. Multi-scale topology optimization. In: 57th AIAA/ASCE/AHS/ASC structures, structural dynamics, and materials conference; 2016. p. 0938.

- [36] Da DC, Cui XY, Long K, Cai Y, Li GY. Multiscale concurrent topology optimization of structures and microscopic multi-phase materials for thermal conductivity. *Eng Computat* 2018.
- [37] Costa M, Sohoulis A, Suleman A. Multi-scale and multi-material topology optimization of gradient lattice structures using surrogate models. *Compos Struct* 2022;115402.
- [38] Liang X, Du J. Concurrent multi-scale and multi-material topological optimization of vibro-acoustic structures. *Comput Meth Appl Mech Eng* 2019;349:117–48.
- [39] Pizzolato A, Sharma A, Maute K, Sciacovelli A, Verda V. Multi-scale topology optimization of multi-material structures with controllable geometric complexity—applications to heat transfer problems. *Comput Meth Appl Mech Eng* 2019;357:112552.
- [40] Yan J, Guo X, Cheng GD. Multi-scale concurrent material and structural design under mechanical and thermal loads. *Comput Mech* 2016;57:437–46.
- [41] Zhou MD, Geng D. Multi-scale and multi-material topology optimization of channel-cooling cellular structures for thermomechanical behaviors. *Comput Meth Appl Mech Eng* 2021;383:113896.
- [42] Wang L, Zhao XY, Liu DL. Size-controlled cross-scale robust topology optimization based on adaptive subinterval dimension-wise method considering interval uncertainties. *Eng Computat* 2022:1–18.
- [43] Bendsoe MP, Sigmund O. *Topology optimization: theory, methods, and applications*. Springer Science & Business Media; 2003.
- [44] Yin L, Ananthasuresh G. Topology optimization of compliant mechanisms with multiple materials using a peak function material interpolation scheme. *Struct Multidiscip Optim* 2001;23:49–62.
- [45] Hvejsel CF, Lund E. Material interpolation schemes for unified topology and multi-material optimization. *Struct Multidiscip Optim* 2011;43:811–25.
- [46] Zuo WJ, Saitou K. Multi-material topology optimization using ordered SIMP interpolation. *Struct Multidiscip Optim* 2017;55:477–91.
- [47] Wang MY, Wang XM. Color level sets: a multi-phase method for structural topology optimization with multiple materials. *Comput Meth Appl Mech Eng* 2004; 193:469–96.
- [48] Wang MY, Chen SK, Wang XM, Mei YL. *Design of multimaterial compliant mechanisms using level-set methods*, (2005).
- [49] Guo X, Zhang WS, Zhong WL. Stress-related topology optimization of continuum structures involving multi-phase materials. *Comput Meth Appl Mech Eng* 2014; 268:632–55.
- [50] Zhuang CG, Xiong ZH, Ding H. Topology optimization of multi-material for the heat conduction problem based on the level set method. *Eng Optim* 2010;42: 811–31.
- [51] Wang YG, Luo YJ, Yan Y. A multi-material topology optimization method based on the material-field series-expansion model. *Struct Multidiscip Optim* 2022;65:1–15.
- [52] Du ZL, Cui TC, Liu C, Zhang WS, Guo YL, Guo X. An efficient and easy-to-extend Matlab code of the Moving Morphable Component (MMC) method for three-dimensional topology optimization. *Struct Multidiscip Optim* 2022;65:1–29.
- [53] Al-Ketan O, Abu Al-Rub RK. Multifunctional mechanical metamaterials based on triply periodic minimal surface lattices. *Adv Eng Mater* 2019;21:1900524.
- [54] Zhang WS, Yuan J, Zhang J, Guo X. A new topology optimization approach based on Moving Morphable Components (MMC) and the ersatz material model. *Struct Multidiscip Optim* 2016;53:1243–60.
- [55] Zhang WS, Li D, Yuan J, Song JF, Guo X. A new three-dimensional topology optimization method based on moving morphable components (MMCs). *Comput Mech* 2017;59:647–65.
- [56] Wang L, Liu Y, Li M. Time-dependent reliability-based optimization for structural-topological configuration design under convex-bounded uncertain modeling. *Reliab Eng Syst Saf* 2022;221:108361.
- [57] Xu ZJ, Wang QH, Li JR. Modeling porous structures with fractal rough topography based on triply periodic minimal surface for additive manufacturing. *Rapid Prototyp J* 2017.
- [58] Gandy PJ, Bardhan S, Mackay AL, Klinowski J. Nodal surface approximations to the P, G, D and I-WP triply periodic minimal surfaces. *Chem Phys Lett* 2001;336: 187–95.
- [59] Han L, Che SN. An overview of materials with triply periodic minimal surfaces and related geometry: from biological structures to self-assembled systems. *Adv Mater* 2018;30:1705708.
- [60] Von Schnering H, Nesper R. Nodal surfaces of Fourier series: fundamental invariants of structured matter. *Zeitschr Phys B Condens Matter* 1991;83:407–12.
- [61] Nguyen BD, Han SC, Jung YC, Kang K. Design of the P-surfaced shellular, an ultralow density material with micro-architecture. *Comput Mater Sci* 2017;139:162–78.
- [62] Al-Ketan O, Al-Rub RKA, Rowshan R. Mechanical properties of a new type of architected interpenetrating phase composite materials. *Adv Mater Technol* 2017; 2:1600235.
- [63] Yang N, Quan Z, Zhang DW, Tian YL. Multi-morphology transition hybridization CAD design of minimal surface porous structures for use in tissue engineering. *Comput-Aided Des* 2014;56:11–21.
- [64] Yoo D-J, Kim K-H. An advanced multi-morphology porous scaffold design method using volumetric distance field and beta growth function. *Int J Precis Eng Manuf* 2015;16:2021–32.
- [65] Arabnejad S, Pasini D. Mechanical properties of lattice materials via asymptotic homogenization and comparison with alternative homogenization methods. *Int J Mech Sci* 2013;77:249–62.
- [66] Fu JJ, Sun PF, Du YX, Li H, Zhou XM, Tian QH. Isotropic design and mechanical characterization of TPMS-based hollow cellular structures. *Compos Struct* 2022; 279:114818.
- [67] Da DC. Inverse homogenization design of lattice structures without scale separation. *Structures*. Elsevier; 2021. p. 796–805.